ACS Catalysis

pubs.acs.org/acscatalysis Research Article

Local Modulation of Single-Atomic Mn Sites for Enhanced Ambient Ammonia Electrosynthesis

Lili Han,○ Machuan Hou,○ Pengfei Ou,○ Hao Cheng, Zhouhong Ren, Zhixiu Liang, J. Anibal Boscoboinik, Adrian Hunt, Iradwikanari Waluyo, Shusheng Zhang, Longchao Zhuo, Jun Song, Xijun Liu,* Jun Luo, and Huolin L. Xin*

Cite This: *ACS Catal.* 2021, 11, 509−516 Read Online

ABSTRACT: Rationally tuning the local structures of single-atomic active sites for the electrocatalytic N_2 reduction reaction (NRR) remains an urgent but worthwhile research topic. Herein, we accomplish the local modulation of single-atomic Mn sites and construct single $Mn-O_3N_1$ sites anchored on porous carbon ($Mn-O_3N_1$/PC) by delicately controlling the Mn−O bonding conditions. The constructed structures are confirmed via the combination of atomic-scale imaging, Raman spectroscopy, synchrotron radiation-based soft and hard X-ray absorption spectroscopies, and X-ray photoelectron spectroscopy. The $Mn-O_3N_1$/PC catalyst yields an NH_3 yield rate of 66.41 $\mu g\ h^{-1}\ mg_{cat.}^{-1}$ (corresponding to 1.56 mg $h^{-1}\ mg_{Mn}^{-1}$) at −0.35 V versus reversible hydrogen electrode, which is about four times that on the control $Mn-N_4$/PC catalyst. The enhanced NRR performance is ascribed to its unique geometry and electronic structures, which not only facilitate the adsorption and activation of the N_2 molecule but also lower the free energy change of the potential-determining step.

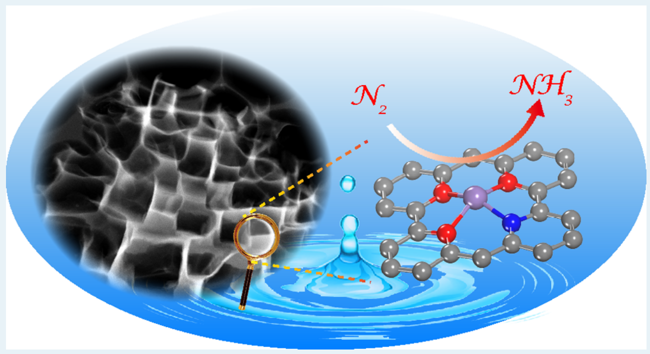

KEYWORDS: *ammonia electrosynthesis, local modulation, single-atom catalyst, Mn sites, ambient condition, N_2 reduction reaction*

INTRODUCTION

Electrocatalytic N_2 reduction reaction (NRR), being a gentle and ambient process with low energy consumption, is a promising alternative to the energy- and resource-intensive Haber−Bosch process for industrial-scale NH_3 production.[1−3] Single-atom catalysts (SACs) with the lowest site size, nearly 100% atomic efficiency, and unique low-coordinated features are expected to have great potential to improve the NRR performance, as confirmed by recent studies (such as Ru,[4,5] Mo,[6] Fe,[7−10] Au,[11] Cu,[12] Y,[13] Sc,[13] and B[14] SACs). Particularly, coordination environments of metal atoms in SACs have a great influence on their electronic structures and subsequently affect their catalytic activity.[15−20] For example, Pan et al. found single Fe atoms anchored by four coordinating N atoms exhibit the highest benzene oxidation reaction performance while the activity decreases gradually upon replacing the coordinated N atoms.[15] Yin and coworkers constructed two Pt SACs of a four-coordinated $C_2-Pt-Cl_2$ species and a five-coordinated $C_1-Pt-Cl_4$ species on graphdiyne, and found that the former configuration has much higher catalytic activity than the later one for the hydrogen evolution reaction.[16] These pioneering research inspire us to modulate the local environment of metal sites in SACs for enhanced NRR performance, which, however, has not been explored before.

Previous studies have indicated that Mn−O sites have a capability of catalyzing NRR because of the proper energy and symmetry 3d orbitals of Mn, which are beneficial for the adsorption and activation of N_2 molecules.[21,22] In addition to our previous study about NRR and SAC catalysis,[6,7,23] we have rationally modulated the local environments of single Mn sites and built atomic $Mn-O_3N_1$ sites anchored on porous carbon ($Mn-O_3N_1$/PC) by delicately controlling the pyrolysis temperature of the Mn−O fragments. $Mn-O_3N_1$/PC and its control sample (single $Mn-N_4$ sites anchored on porous carbon, namely $Mn-N_4$/PC) were synthesized by a dissolution-and-carbonization method. In the synthesis of $Mn-O_3N_1$/PC, the Mn precursors were efficiently embedded into the glucose backbones during the dissolution, which ensured a

Received: September 18, 2020
Revised: November 2, 2020
Published: December 24, 2020

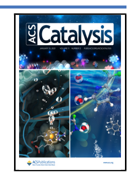

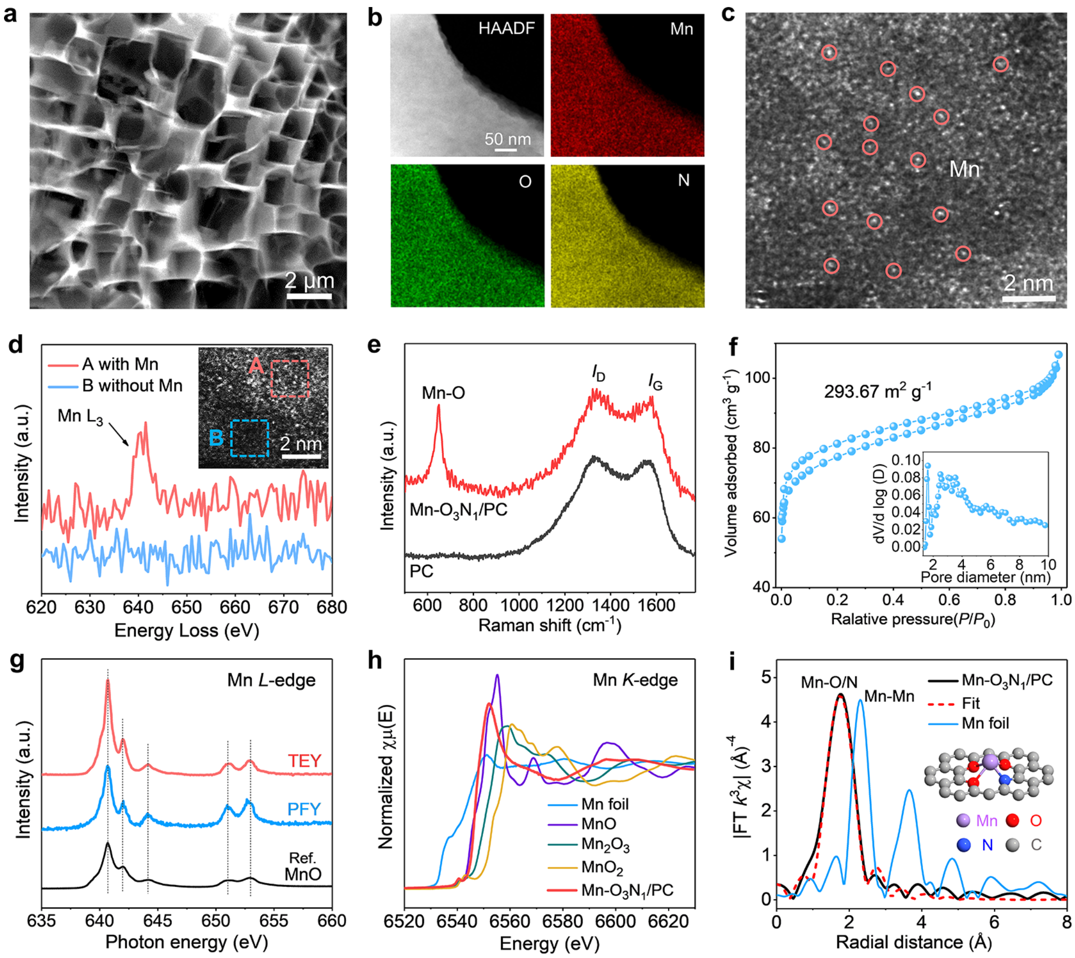

Figure 1. Structural characterization of Mn−O_3N_1/PC. (a) Low-magnification HAADF-STEM image. (b) HAADF-STEM image and corresponding STEM−EDS elemental maps of Mn, O, and N. (c) Atomic-resolution HAADF-STEM image, in which some of the single-atomic sites are highlighted by red circles. (d) EELS spectra in areas A with Mn atoms and B without Mn ones. (e) Raman spectra of Mn−O_3N_1/PC and PC. (f) N_2 physisorption isotherm. The inset is the corresponding pore size distribution. (g) Mn L-edge TEY and PFY spectra of Mn−O_3N_1/PC and the reference spectrum of MnO. (h) Normalized XANES spectra at the Mn K-edge of Mn foil, MnO, Mn_2O_3, MnO_2, and Mn−O_3N_1/PC. (i) FT-EXAFS spectra of Mn foil, Mn−O_3N_1/PC, and the curve fitting with the Mn−O_3N_1/graphene. The inset is the corresponding atomic model.

homogeneous distribution of the Mn centers in the subsequent carbonization.[24,25] Subsequently, the carbon from carbonization of the glucose was etched by NH_3 produced via the decomposition of hydroxylamine hydrochloride precursor to form N-doped 3-dimensional (3D) PC frameworks.[26] Finally, the single Mn atoms were anchored on the 3D frameworks through Mn−O−C and Mn−N−C bondings at 700 °C because of a strong metal−N/O binding effect, resulting in Mn−O_3N_1/PC.[27−29] Because the O atoms on the carbon substrate are more vulnerable to be replaced by N atoms at an elevated temperature,[21,30,31] Mn−N_4 single sites tend to be generated at a higher temperature by the substitution of O with N atoms. Therefore, for comparison, Mn−N_4/PC was prepared under conditions similar to Mn−O_3N_1/PC except that the pyrolysis temperature was set at 900 °C.

■ RESULTS AND DISCUSSION

The obtained Mn−O_3N_1/PC can be directly observed using a scanning electron microscope and a transmission electron microscope. Figures 1a and S1a,b present its feature of interconnected carbon frameworks with a randomly opened porous structure. Furthermore, elemental maps acquired using energy-dispersive X-ray spectroscopy (EDS) shown in Figures 1b and S1c manifest the homogenous distribution of Mn, O, N, and C over the entire architectures. The high-resolution TEM image, selected area electron diffraction pattern, and X-ray diffraction pattern in Figure S1d−f demonstrate the amorphousness of Mn−O_3N_1/PC, indicating no Mn-related crystals existing in the sample. Atomic-resolution aberration-corrected high-angle annular dark-field scanning transmission electron microscopy (HAADF-STEM) images in Figures 1c and S2 display many isolated bright dots with an average size of 0.18 ± 0.05 nm (Figure S3), distributed on the carbon matrix. The dots are identified by electron energy-loss spectroscopy (EELS) analysis to be Mn atoms (Figure 1d). The Raman peak at 647 cm^{-1} in Figure 1e is assigned to the Mn−O vibration,[32] suggesting binding of the Mn to O. The N_2 physisorption isotherm and pore size distribution in Figure 1f demonstrate its high specific area of 293.67 m^2 g^{-1} and mesopore structure, which are beneficial to exposure of the isolated Mn sites and the mass transport of electrolytes during electrolysis.[33]

Synchrotron radiation-based soft and hard X-ray absorption spectroscopies (XAS) were employed to study the oxidation state and local structure of Mn in Mn−O_3N_1/PC. Figure 1g shows that Mn L-edge soft XAS in the total electron yield

Table 1. Best-Fit Structural Parameters Derived from the Analyses of the Mn K-Edge XANES Spectrum of $Mn-O_3N_1/PC$[a]

structure	bond-type	R_XANES (Å)	R_DFT (Å)	*D*	R_{sq}
$Mn-O_3N_1$	Mn−N	2.13	1.98	**2.034**	**0.0109**
	Mn−O	2.28, 2.29, 2.29	2.12, 2.13, 2.13		
$Mn-O_2N_2'$	Mn−N	2.13, 2.13	1.87, 1.87	2.569	0.0147
	Mn−O	2.26, 2.26	1.98, 1.98		
$Mn-O_2N_2''$	Mn−N	2.15, 2.15	1.89, 1.89	2.500	0.0143
	Mn−O	2.23, 2.23	1.96, 1.96		
$Mn-O_2N_2'''$	Mn−N	2.28, 2.28	2.00, 2.00	2.618	0.0150
	Mn−O	2.41, 2.41	2.11, 2.11		
$Mn-O_1N_3$	Mn−N	2.14, 2.17, 2.20	1.88, 1.90, 1.93	2.618	0.0150
	Mn−O	2.26	1.98		
$Mn-O_4$	Mn−O	2.64, 2.64, 2.64, 2.64	2.38, 2.38, 2.38, 2.38	2.413	0.0138
$Mn-O_3C_1$	Mn−C	2.16	1.96	2.798	0.0162
	Mn−O	2.34, 2.40, 2.40	2.13, 2.18, 2.18		
$Mn-O_2C_2'$	Mn−C	2.05, 2.05	1.86, 1.86	4.162	0.0339
	Mn−O	2.26, 2.26	2.05, 2.05		
$Mn-O_2C_2''$	Mn−C	2.15, 2.15	1.89, 1.89	3.021	0.0191
	Mn−O	2.28, 2.28	2.00, 2.00		
$Mn-O_2C_2'''$	Mn−C	2.10, 2.10	1.91, 1.91	3.559	0.0263
	Mn−O	2.16, 2.16	1.96, 1.96		
$Mn-O_1C_3$	Mn−C	2.18, 2.19, 2.27	1.91, 1.92, 1.99	3.211	0.0205
	Mn−O	2.39	2.10		

[a]The models of $Mn-O_xN_y$ and $Mn-O_xC_y$ structures for the fit were generated after energy optimization. Note: *R*_XANES is the fitted bond length from XANES calculations; *R*_DFT is the calculated bond length from the DFT results; *D* and R_{sq} are the total metric distance and square residue function, which represent the agreement between the XANES calculations and experimental spectrum (the smaller, the better).

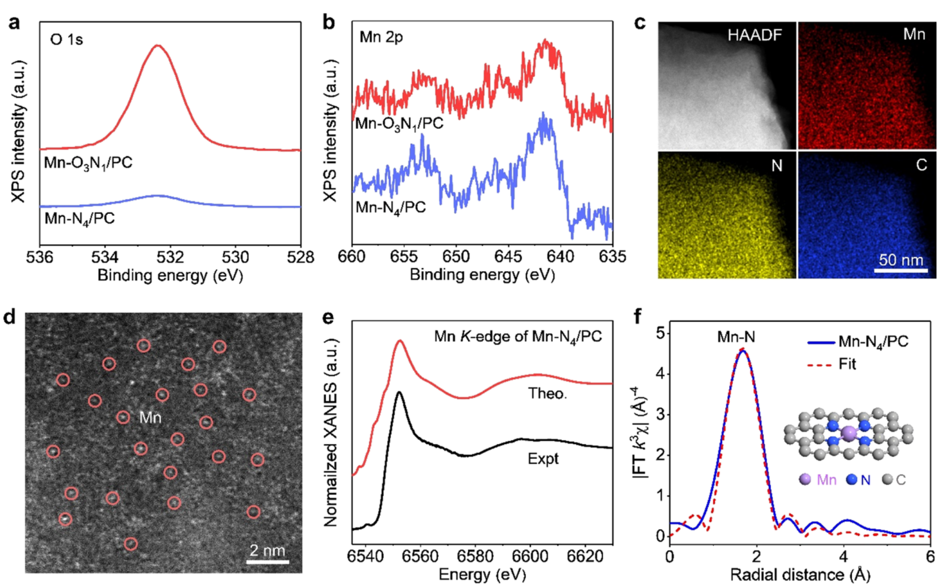

Figure 2. Structural characterization of $Mn-N_4/PC$. (a) O 1s and (b) Mn 2p spectra of $Mn-O_3N_1/PC$ and $Mn-N_4/PC$. (c) HAADF-STEM image and the corresponding STEM−EDS elemental maps of Mn, N, and C. (d) Atomic-resolution HAADF-STEM image of $Mn-N_4/PC$. (e) Comparison between the experimental Mn K-edge XANES spectrum of $Mn-N_4/PC$ and the theoretical one calculated based on the model of $Mn-N_4$/graphene, which was generated after energy optimization. (f) FT-EXAFS spectrum of $Mn-N_4/PC$ and curve fitting with the $Mn-N_4$/graphene model. The inset is the corresponding atomic model.

(TEY) mode is similar to the one in the partial fluorescence yield (PFY) mode, indicating the uniform distribution of Mn on the surface and in the bulk of $Mn-O_3N_1/PC$ because signals within 5−10 nm thickness of the sample surface and up to 100 nm thickness of bulk are detected in TEY and PFY modes, respectively.[34,35] The comparison of the Mn L-edge spectra of $Mn-O_3N_1/PC$ and MnO reference suggests that the oxidation state of Mn in $Mn-O_3N_1/PC$ is +2. This result is further confirmed by the comparison of Mn K-edge X-ray absorption near-edge structure (XANES) spectra of Mn foil, MnO, Mn_2O_3, MnO_2, and $Mn-O_3N_1/PC$ (Figure 1h), where the pre-edge for $Mn-O_3N_1/PC$ is close to that for MnO.

The Fourier transform (FT) k^3-weighted EXAFS spectra in Figure 1i show that, for $Mn-O_3N_1/PC$, only a primary peak at 1.76 Å can be observed, without the signal of the Mn−Mn shell (compared with Mn foil), which further proves that the Mn atoms are isolated from each other. EXAFS fitting analysis indicates four-coordinate Mn centers in $Mn-O_3N_1/PC$, that

https://dx.doi.org/10.1021/acscatal.0c04102
ACS Catal. 2021, 11, 509−516

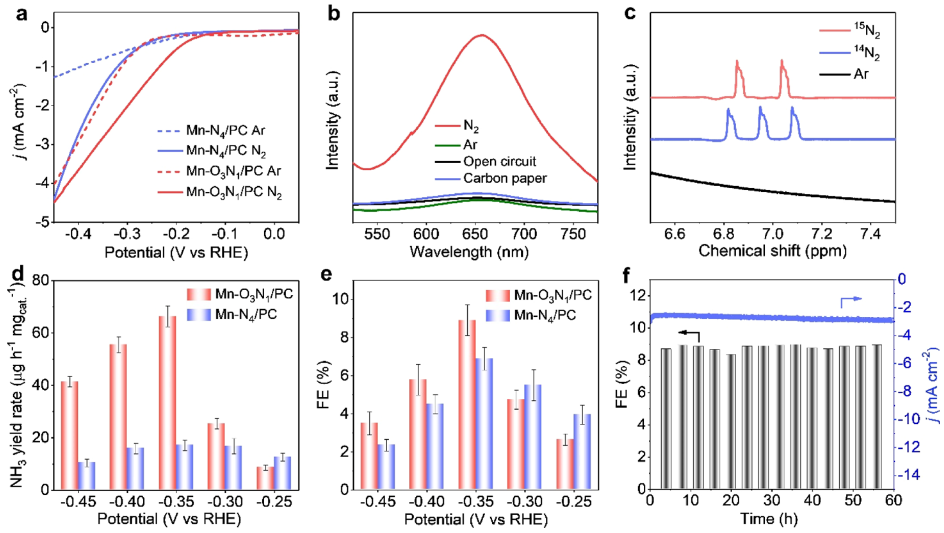

Figure 3. NRR electrochemical performances of Mn−O_3N_1/PC and Mn−N_4/PC in 0.1 M HCl. (a) Linear sweep voltammetric curves of Mn−O_3N_1/PC and Mn−N_4/PC in Ar- (red line) and N_2-saturated (blue line) HCl solutions, in which j denotes the current density. (b) UV−vis absorption spectra of electrolytes stained with an indophenol blue indicator after NRR on Mn−O_3N_1/PC, carbon paper, Ar control experiment, and under open circuit conditions at −0.35 V. (c) ^1H NMR spectra of 0.1 M HCl solutions after 2 h electrochemical reduction in 0.1 M HCl at −0.35 V using Ar (in black), $^{14}N_2$ (in blue), and $^{15}N_2$ (in red) as the feeding gases. (d) NH_3 yield rates and (e) FEs of Mn−O_3N_1/PC and Mn−N_4/PC at each given potential. (f) FE (black) and chronoamperometric curve (blue) stabilities of Mn−O_3N_1/PC.

is, Mn−X_4 (X = C, N, and O), whereas it is difficult to discern C, N, and O coordinates by the fitting. To further identify the local structure of Mn−O_3N_1/PC, XANES simulations with high sensitivity to the 3D atom arrangement have been performed with various theoretically optimized models of Mn−O_xN_y and Mn−O_xC_y ($x + y = 4$) structures based on the results of four-coordinate Mn centers from EXAFS fitting in Figure 1i and Mn−O bonding from Raman analysis in Figure 1e. It turns out that, among all the structural models, the Mn−O_3N_1 one has the best agreement with the experimental spectra because it has been demonstrated to have the best fit at XANES fitting and the smallest deviation from density functional theory (DFT) results (Table 1 and Figure S4). Furthermore, we fit the EXAFS spectrum of Mn−O_3N_1/PC with the Mn−O_3N_1 model. The fitting result shows that the simulated EXAFS spectrum is nearly identical to the experimental one (Figure 1i and Table S1).

X-ray photoelectron spectroscopy was used to explore electronic structures of Mn−O_3N_1/PC and its control sample (Mn−N_4/PC). Compared with Mn−O_3N_1/PC, the amount of O in Mn−N_4/PC decreases sharply (Figure 2a), while the amount of Mn is almost kept (Figure 2b). Additionally, the Mn−O Raman peak at −647 cm^{-1} is absent (Figure S5a). These results indicate that the local environment of Mn is changing during heating from 700 to 900 °C. Further characterization of Mn−N_4/PC demonstrates its hierarchically porous structure with atomically dispersed Mn distribution on N-doped carbon (Figures S5b,c and 2c,d). Mn loading in Mn−N_4/PC measured by inductively coupled plasma atomic emission spectroscopy analysis is 4.35 wt %, close to the one (3.85 wt %) in Mn−O_3N_1/PC, while the specific area (542.92 m^2 g^{-1}) of Mn−N_4/PC is around twice that of the Mn−O_3N_1/PC (293.67 m^2 g^{-1}) (Figure S5d). XANES and EXAFS fitting results in Figure 2e,f and Table S1 suggest that the single Mn atoms coordinate with four N atoms on the carbon substrate. The identification of the isolated Mn−O_3N_1 and Mn−N_4 sites above confirms the realization of local modulation of single-atomic Mn sites.

The NRR tests were performed on Mn−O_3N_1/PC and Mn−N_4/PC. Before each NRR test, N_2 ($^{14}N_2$ or $^{15}N_2$) and Ar gases used in the experiment were purified by 2 M NaOH, 0.1 M $FeSO_4$, and 5 mM H_2SO_4 solutions to exclude the possible interferences of NH_3 and NO_x in the feeding gases.[36] The current density enhancement under N_2 over the ones under Ar indicates that both Mn−O_3N_1/PC and Mn−N_4/PC are active for NRR catalysis (Figure 3a). The concentration of produced NH_3 was estimated by the widely adopted method of indophenol blue.[37] After electrolysis in N_2-saturated 0.1 M HCl solution at −0.35 V versus reversible hydrogen electrode (vs RHE; all potentials below are vs RHE unless stated), the corresponding ultraviolet−visible (UV−vis) absorption spectrum (Figure 3b, red curve) shows distinctive absorption at 657 nm on Mn−O_3N_1/PC, concretely confirming the occurrence of the NRR process on Mn−O_3N_1/PC. Importantly, controlled experiments and isotope measurements were performed to exclude contamination from exotic NH_3 according to the reported rigorous protocol.[36] First, when the NRR experiment was performed by feeding Ar while keeping other reaction parameters unchanged, no NH_3 was detected (Figures 3b and S6). We conducted the same NRR experiment solely on carbon paper, where no NH_3 was produced. Similarly, when we placed the catalyst in the N_2-saturated electrolyte for 2 h without electrolysis (i.e., open circuit), no NH_3 was measured. Furthermore, a ^{15}N isotopic labeling experiment has been performed to verify the nitrogen source of the produced NH_3 (Figure 3c). The ^1H nuclear magnetic resonance (^1H NMR) spectra show a triplet coupling for $^{14}NH_4^+$ and a double coupling for $^{15}NH_4^+$, indicating that the detected NH_3 is exclusively produced from the reduction of the introduced N_2.

The NRR activity of Mn−O_3N_1/PC is compared with that of Mn−N_4/PC. Their dependence of faradaic efficiencies (FEs) and NH_3 yield rates on given applied potentials is shown in Figure 3d,e, respectively. It can be seen that the maximum FE of 8.91 ± 0.82% with a remarkable yield rate of 66.41 ± 4.05 $\mu g\ h^{-1}\ mg_{cat.}^{-1}$ (corresponding to 1.56 $mg\ h^{-1}\ mg_{Mn}^{-1}$)

https://dx.doi.org/10.1021/acscatal.0c04102
ACS Catal. 2021, 11, 509−516

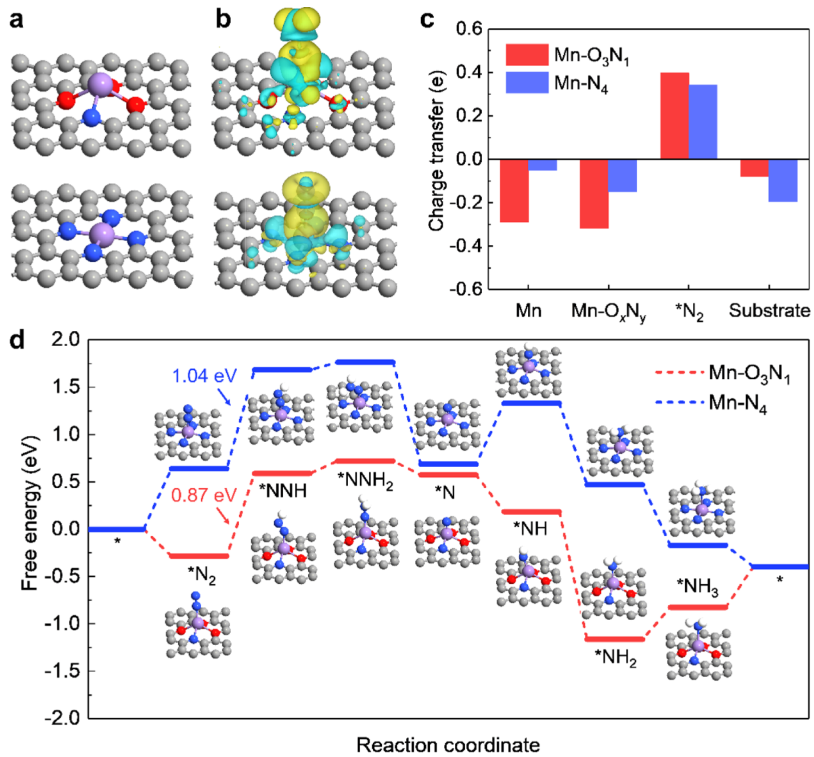

Figure 4. DFT calculation results of Mn−O_3N_1 and Mn−N_4. (a) Optimized geometries of Mn−O_3N_1/graphene (top) and Mn−N_4/graphene (bottom). (b) Contour plots of the charge density difference of N_2 adsorbed at the top site on Mn−O_3N_1/graphene (top) and Mn−N_4/graphene (bottom). The light yellow- and blue-shaded regions indicate the electron accumulation and depletion, respectively. (c) Charge transfer determined by the Bader charge analysis between Mn−O_3N_1/graphene or Mn−N_4/graphene, adsorbed intermediate of *N_2, and substrate of PC. (d) Free energy diagram of the electrochemical NRR via an associative distal pathway on the Mn−O_3N_1/graphene and the Mn−N_4/graphene, together with the corresponding geometries of the reaction intermediates, respectively. The white, gray, blue, red, and purple spheres represent H, C, N, O, and Mn atoms, respectively. Each asterisk (*) represents an adsorbed reactive intermediate on an active site or a vacant active site.

for NH_3 is achieved at −0.35 V on Mn−O_3N_1/PC. Besides, no N_2H_4 is detected as a byproduct (Figure S7). By contrast, the FE and yield rate of Mn−N_4/PC with a similar Mn loading yet a higher specific area are 6.89 ± 0.62% and 17.13 ± 2.01 μg h^{-1} $mg_{cat.}^{-1}$ (corresponding to 0.39 mg h^{-1} mg_{Mn}^{-1}) at −0.35 V, respectively, less than those of Mn−O_3N_1/PC. Besides, the PC substrate has a low maximum NH_3 yield rate and FEs of 3.64 ± 0.5% and 5.92 ± 0.81 μg h^{-1} $mg_{cat.}^{-1}$ (Figure S8). These results demonstrate that the Mn−O_3N_1 site is more active than the Mn−N_4 one for NRR to NH_3. Moreover, the NRR current density and the FE remained essentially stable during 60 h electrolysis at −0.35 V (Figure 3f). The characterization of Mn−O_3N_1/PC after the electrolysis in Figures S9 and S10 demonstrates the good stability of the single Mn sites during the NRR test, which agrees well with its robust catalytic property for NRR.

To further elucidate the intrinsic reason for the superior catalytic activity of the Mn−O_3N_1 site over the Mn−N_4 one for NH_3 production, DFT calculations were performed to first study the adsorption of N_2 on both Mn−O_3N_1/graphene and Mn−N_4/graphene. It is revealed that Mn−O_3N_1 exhibits significantly stronger binding (−0.83 eV) with N_2 than Mn−N_4 (0.09 eV). The higher binding strength between Mn−O_3N_1 and N_2 can be attributed to combinatory effects of local binding geometry and atomic electronegativity. Examining the local binding geometries of N_2 at Mn−O_3N_1 and Mn−N_4 (Figure 4a), we can see that the single Mn atom in Mn−O_3N_1 stretches outward from the plane and thus only the top site is available for adsorption, which is in contrast with the in-plane structure of Mn−N_4 (Figure 4a). On the other hand, the larger electronegativity of O enables more negative charges to transfer from Mn to O, and therefore, rendering Mn in Mn−O_3N_1 more active in the first reaction step of the NRR process, that is, to polarize and activate the N_2 molecule. Contour plots of charge density difference of N_2 adsorption at Mn−O_3N_1 and Mn−N_4 (Figure 4b) clearly illustrate that charges are localized and transferred from the positively charged Mn atom to N_2, resulting in the formation of a N−Mn bond and the notable weakening of the N≡N triple bond. However, for the case of Mn−N_4, the negative charges are shared by the anchoring nitrogen atoms, thus lowering the localization around the Mn atom. This is also evidenced by the Bader charge analysis,[38,39] more electrons are transferred from Mn−O_3N_1 to the adsorbed N_2 molecule (0.32 e) compared with that of Mn−N_4 (0.15 e), as summarized in Figure 4c.

Furthermore, DFT calculations were also performed to map out the reaction free energy diagram of NRR over Mn−O_3N_1 and Mn−N_4 sites (see Table S2 for more details). As shown in Figure 4d, for Mn−O_3N_1, the potential-determining step (PDS) is the reductive protonation of adsorbed N_2 with a ΔG_{PDS} of 0.87 eV without external potential, lower than the ΔG_{PDS} (1.04 eV) on Mn−N_4. Overall, DFT calculations suggest that the enhanced catalytic performance on Mn−O_3N_1 can be attributed to the synergy of enhanced N_2 adsorption (to initiate the NRR process) and stabilization of *NNH (a lower ΔG_{PDS}). We further note that the Mn-N_xO_{4-x}/graphene moieties ($0 \leq x \leq 3$) generally exhibit good performance in catalyzing NRR, yet their effectiveness is much dependent on

https://dx.doi.org/10.1021/acscatal.0c04102
ACS Catal. 2021, 11, 509−516

the number of coordinated O atoms, with $Mn-O_3N_1$/graphene possessing the highest activity (see Figure S11 for more details).

In situ attenuated total reflectance surface-enhanced infrared absorption spectroscopy measurements were conducted to detect possible reaction intermediates during the NRR on $Mn-O_3N_1$/PC. As shown in Figure S12, three positive bands at 1425, 1284, and 1118 cm^{-1} are attributed to the N−H,[40] $-NH_2$ wagging,[41] and N−N stretching[42] of adsorbed N_2H_y species, respectively, suggesting the formation of $*N_2H_y$ ($1 < y < 4$) on the catalyst surface. When $*N_2H_4$ is formed, there are two possible consequent pathways. Pathway 1 involves a four-electron transfer, where $*N_2H_4$ desorbs from $Mn-O_3N_1$/PC and enters into the solution. In contrast, pathway 2 is a six-electron transfer process, where a pair of proton and electron is first transferred to $*N_2H_4$ and reduce it to $*NH_2$ with a release of a free NH_3 molecule. Then, the formed $*NH_2$ is further reduced to produce the second NH_3 molecule by adding another pair of proton and electron. Because the hydrazine was not detected in the products of NRR (Figure S7), it can be deduced that the NRR proceeds in pathway 2. The intermediates above are consistent with the ones from the DFT calculation results on $Mn-O_3N_1$ (Figure 4d).

In summary, we accomplished the local modulation of single-atomic Mn sites by delicately regulating the breaking of the Mn−O bond and built single $Mn-O_3N_1$ sites on PC for ambient NH_3 electrosynthesis. The $Mn-O_3N_1$ catalyst reached an FE of 8.91% and a fairly high NH_3 yield rate of 66.41 $\mu g\ h^{-1}\ mg_{cat.}^{-1}$ (corresponding to 1.56 $mg\ h^{-1}\ mg_{Mn}^{-1}$) at −0.35 V in 0.1 M HCl, superior to the control $Mn-N_4$ catalyst. Moreover, the catalyst exhibits remarkable stability with neither obvious current drop nor large FE fluctuation for 60 h electrolysis. DFT calculations reveal that the enhanced catalytic performance of $Mn-O_3N_1$ can be attributed to the synergy of enhanced N_2 adsorption (to initiate the NRR process) and stabilization of *NNH (a lower ΔG_{PDS}). This work may inspire new exploration and design of stable and efficient SACs with a specific coordination environment.

■ ASSOCIATED CONTENT

Supporting Information

The Supporting Information is available free of charge at https://pubs.acs.org/doi/10.1021/acscatal.0c04102.

Additional experimental methods, materials characterization, and electrochemical measurements (PDF)

■ AUTHOR INFORMATION

Corresponding Authors

Xijun Liu − *Institute for New Energy Materials & Low-Carbon Technologies and Tianjin Key Lab of Photoelectric Materials & Devices, School of Materials Science and Engineering, Tianjin University of Technology, Tianjin 300384, China;* orcid.org/0000-0002-2624-6901; Email: xjliu@tjut.edu.cn

Huolin L. Xin − *Department of Physics and Astronomy, University of California Irvine, Irvine, California 92697, United States;* orcid.org/0000-0002-6521-868X; Email: huolinx@uci.edu

Authors

Lili Han − *Institute for New Energy Materials & Low-Carbon Technologies and Tianjin Key Lab of Photoelectric Materials & Devices, School of Materials Science and Engineering, Tianjin University of Technology, Tianjin 300384, China; Department of Physics and Astronomy, University of California Irvine, Irvine, California 92697, United States*

Machuan Hou − *Institute for New Energy Materials & Low-Carbon Technologies and Tianjin Key Lab of Photoelectric Materials & Devices, School of Materials Science and Engineering, Tianjin University of Technology, Tianjin 300384, China*

Pengfei Ou − *Department of Mining and Materials Engineering, McGill University, Montreal H3A 0C5, Canada*

Hao Cheng − *Department of Physics and Astronomy, University of California Irvine, Irvine, California 92697, United States*

Zhouhong Ren − *Institute for New Energy Materials & Low-Carbon Technologies and Tianjin Key Lab of Photoelectric Materials & Devices, School of Materials Science and Engineering, Tianjin University of Technology, Tianjin 300384, China*

Zhixiu Liang − *Department of Chemistry, Stony Brook University, Stony Brook, New York 11794, United States*

J. Anibal Boscoboinik − *Center for Functional Nanomaterials, Brookhaven National Laboratory, Upton, New York 11973, United States;* orcid.org/0000-0002-5090-7079

Adrian Hunt − *National Synchrotron Light Source II, Brookhaven National Laboratory, Upton, New York 11973, United States*

Iradwikanari Waluyo − *National Synchrotron Light Source II, Brookhaven National Laboratory, Upton, New York 11973, United States;* orcid.org/0000-0002-4046-9722

Shusheng Zhang − *College of Chemistry, Zhengzhou University, Zhengzhou 450000, China;* orcid.org/0000-0003-3983-2894

Longchao Zhuo − *School of Materials Science and Engineering, Xi'an University of Technology, Xi'an 710048, China;* orcid.org/0000-0003-3396-3893

Jun Song − *Department of Mining and Materials Engineering, McGill University, Montreal H3A 0C5, Canada;* orcid.org/0000-0003-3675-574X

Jun Luo − *Institute for New Energy Materials & Low-Carbon Technologies and Tianjin Key Lab of Photoelectric Materials & Devices, School of Materials Science and Engineering, Tianjin University of Technology, Tianjin 300384, China;* orcid.org/0000-0001-5084-2087

Complete contact information is available at: https://pubs.acs.org/10.1021/acscatal.0c04102

Author Contributions

○L.H., M.H., and P.O. contributed equally.

Notes

The authors declare no competing financial interest.

■ ACKNOWLEDGMENTS

This work was financially supported by National Key R&D Program of China (2017YFA0700104), National Natural Science Foundation of China (22075211, 21601136, 51971157, and 51761165012), Tianjin Science Fund for Distinguished Young Scholars (19JCJQJC61800), and Science and Technology Development Fund of Tianjin Education Commission for Higher Education (No. 2018KJ126). Work done at UCI was supported by the startup funding of H.L.X. This research used resources of the Center for Functional

Nanomaterials, which is a U.S. Department of Energy (DOE) Office of Science Facility, and the 7-BM and 23-ID-2 beamlines of the National Synchrotron Light Source II, a U.S. DOE Office of Science User Facility operated for the DOE Office of Science by Brookhaven National Laboratory under contract no. DE-SC0012704. H.L.X. would like to acknowledge Prof. Frank de Groot, Prof. Way-Faung Pong and Dr. Hsiao-Tsu Wang's inputs on the Mn s-XAS.

REFERENCES

(1) Cheng, H.; Ding, L. X.; Chen, G. F.; Zhang, L.; Xue, J.; Wang, H. Molybdenum Carbide Nanodots Enable Efficient Electrocatalytic Nitrogen Fixation under Ambient Conditions. *Adv. Mater.* **2018**, *30*, 1803694.
(2) Hao, Y.-C.; Guo, Y.; Chen, L.-W.; Shu, M.; Wang, X.-Y.; Bu, T.-A.; Gao, W.-Y.; Zhang, N.; Su, X.; Feng, X.; Zhou, J.-W.; Wang, B.; Hu, C.-W.; Yin, A.-X.; Si, R.; Zhang, Y.-W.; Yan, C.-H. Promoting Nitrogen Electroreduction to Ammonia with Bismuth Nanocrystals and Potassium Cations in Water. *Nat. Catal.* **2019**, *2*, 448−456.
(3) Zheng, J.; Lyu, Y.; Qiao, M.; Veder, J. P.; Marco, R. D.; Bradley, J.; Wang, R.; Li, Y.; Huang, A.; Jiang, S. P.; Wang, S. Tuning the Electron Localization of Gold Enables the Control of Nitrogen-to-Ammonia Fixation. *Angew. Chem., Int. Ed.* **2019**, *58*, 18604−18609.
(4) Tao, H.; Choi, C.; Ding, L.-X.; Jiang, Z.; Han, Z.; Jia, M.; Fan, Q.; Gao, Y.; Wang, H.; Robertson, A. W.; Hong, S.; Jung, Y.; Liu, S.; Sun, Z. Nitrogen Fixation by Ru Single-Atom Electrocatalytic Reduction. *Chem* **2019**, *5*, 204−214.
(5) Geng, Z.; Liu, Y.; Kong, X.; Li, P.; Li, K.; Liu, Z.; Du, J.; Shu, M.; Si, R.; Zeng, J. Achieving a Record-High Yield Rate of 120.9 μg_{NH3} $mg_{cat.}^{-1}$ h^{-1} for N_2 Electrochemical Reduction over Ru Single-Atom Catalysts. *Adv. Mater.* **2018**, *30*, 1803498.
(6) Han, L.; Liu, X.; Chen, J.; Lin, R.; Liu, H.; Lü, F.; Bak, S.; Liang, Z.; Zhao, S.; Stavitski, E.; Luo, J.; Adzic, R. R.; Xin, H. L. Atomically Dispersed Molybdenum Catalysts for Efficient Ambient Nitrogen Fixation. *Angew. Chem., Int. Ed.* **2019**, *58*, 2321−2325.
(7) Lü, F.; Zhao, S.; Guo, R.; He, J.; Peng, X.; Bao, H.; Fu, J.; Han, L.; Qi, G.; Luo, J.; Tang, X.; Liu, X. Nitrogen-Coordinated Single Fe Sites for Efficient Electrocatalytic N_2 Fixation in Neutral Media. *Nano Energy* **2019**, *61*, 420−427.
(8) Wang, M.; Liu, S.; Qian, T.; Liu, J.; Zhou, J.; Ji, H.; Xiong, J.; Zhong, J.; Yan, C. Over 56.55% Faradaic Efficiency of Ambient Ammonia Synthesis Enabled by Positively Shifting the Reaction Potential. *Nat. Commun.* **2019**, *10*, 341.
(9) Li, J.; Chen, S.; Quan, F.; Zhan, G.; Jia, F.; Ai, Z.; Zhang, L. Accelerated Dinitrogen Electroreduction to Ammonia via Interfacial Polarization Triggered by Single-Atom Protrusions. *Chem* **2020**, *6*, 885−901.
(10) Zhang, S.; Jin, M.; Shi, T.; Han, M.; Sun, Q.; Lin, Y.; Ding, Z.; Zheng, L. R.; Wang, G.; Zhang, Y.; Zhang, H.; Zhao, H. Electrocatalytically Active Fe-$(O\text{-}C_2)_4$ Single-Atom Sites for Efficient Reduction of Nitrogen to Ammonia. *Angew. Chem., Int. Ed.* **2020**, *59*, 13423−13429.
(11) Qin, Q.; Heil, T.; Antonietti, M.; Oschatz, M. Single-Site Gold Catalysts on Hierarchical N-Doped Porous Noble Carbon for Enhanced Electrochemical Reduction of Nitrogen. *Small Methods* **2018**, *2*, 1800202.
(12) Zang, W.; Yang, T.; Zou, H.; Xi, S.; Zhang, H.; Liu, X.; Kou, Z.; Du, Y.; Feng, Y. P.; Shen, L.; Duan, L.; Wang, J.; Pennycook, S. J. Copper Single Atoms Anchored in Porous Nitrogen-Doped Carbon as Efficient pH-Universal Catalysts for the Nitrogen Reduction Reaction. *ACS Catal.* **2019**, *9*, 10166−10173.
(13) Liu, J.; Kong, X.; Zheng, L.; Guo, X.; Liu, X.; Shui, J. Rare Earth Single-Atom Catalysts for Nitrogen and Carbon Dioxide Reduction. *ACS Nano* **2020**, *14*, 1093−1101.
(14) Ling, C.; Niu, X.; Li, Q.; Du, A.; Wang, J. Metal-Free Single Atom Catalyst for N_2 Fixation Driven by Visible Light. *J. Am. Chem. Soc.* **2018**, *140*, 14161−14168.
(15) Pan, Y.; Chen, Y.; Wu, K.; Chen, Z.; Liu, S.; Cao, X.; Cheong, W.-C.; Meng, T.; Luo, J.; Zheng, L.; Liu, C.; Wang, D.; Peng, Q.; Li, J.; Chen, C. Regulating the Coordination Structure of Single-Atom Fe-N_xC_y Catalytic Sites for Benzene Oxidation. *Nat. Commun.* **2019**, *10*, 4290.
(16) Yin, X.-P.; Wang, H.-J.; Tang, S.-F.; Lu, X.-L.; Shu, M.; Si, R.; Lu, T.-B. Engineering the Coordination Environment of Single-Atom Platinum Anchored on Graphdiyne for Optimizing Electrocatalytic Hydrogen Evolution. *Angew. Chem., Int. Ed.* **2018**, *57*, 9382−9386.
(17) Fei, H.; Dong, J.; Chen, D.; Hu, T.; Duan, X.; Shakir, I.; Huang, Y.; Duan, X. Single Atom Electrocatalysts Supported on Graphene or Graphene-Like Carbons. *Chem. Soc. Rev.* **2019**, *48*, 5207−5241.
(18) Liu, W.; Zhang, L.; Liu, X.; Liu, X.; Yang, X.; Miao, S.; Wang, W.; Wang, A.; Zhang, T. Discriminating Catalytically Active FeN_x Species of Atomically Dispersed Fe−N−C Catalyst for Selective Oxidation of the C−H Bond. *J. Am. Chem. Soc.* **2017**, *139*, 10790−10798.
(19) Wang, X.; Chen, Z.; Zhao, X.; Yao, T.; Chen, W.; You, R.; Zhao, C.; Wu, G.; Wang, J.; Huang, W.; Yang, J.; Hong, X.; Wei, S.; Wu, Y.; Li, Y. Regulation of Coordination Number over Single Co Sites: Triggering the Efficient Electroreduction of CO_2. *Angew. Chem., Int. Ed.* **2018**, *57*, 1944−1948.
(20) Li, X.; Rong, H.; Zhang, J.; Wang, D.; Li, Y. Modulating the Local Coordination Environment of Single-Atom Catalysts for Enhanced Catalytic Performance. *Nano Res.* **2020**, *13*, 1842−1855.
(21) Wang, Z.; Gong, F.; Zhang, L.; Wang, R.; Ji, L.; Liu, Q.; Luo, Y.; Guo, H.; Li, Y.; Gao, P.; Shi, X.; Li, B.; Tang, B.; Sun, X. Electrocatalytic Hydrogenation of N_2 to NH_3 by MnO: Experimental and Theoretical Investigations. *Small Methods* **2019**, *6*, 1801182.
(22) Zhang, L.; Xie, X.-Y.; Wang, H.; Ji, L.; Zhang, Y.; Chen, H.; Li, T.; Luo, Y.; Cui, G.; Sun, X. Boosting Electrocatalytic N_2 Reduction by MnO_2 with Oxygen Vacancies. *Chem. Commun.* **2019**, *55*, 4627−4630.
(23) Han, L.; Song, S.; Liu, M.; Yao, S.; Liang, Z.; Cheng, H.; Ren, Z.; Liu, W.; Lin, R.; Qi, G.; Liu, X.; Wu, Q.; Luo, J.; Xin, H. L. Stable and Efficient Single-Atom Zn Catalyst for CO_2 Reduction to CH_4. *J. Am. Chem. Soc.* **2020**, *142*, 12563−12567.
(24) Gallagher, P. K.; Schrey, F.; Prescott, B. The Thermal Decomposition of Aqueous Manganese (II) Nitrate Solution. *Thermochim. Acta* **1971**, *2*, 405−412.
(25) Han, L.; Ren, Z.; Ou, P.; Cheng, H.; Rui, N.; Lin, L.; Liu, X.; Zhuo, L.; Song, J.; Sun, J.; Luo, J.; Xin, H. L. Modulating Single-Atom Palladium Sites with Copper for Enhanced Ambient Ammonia Electrosynthesis. *Angew. Chem., Int. Ed.* **2020**, DOI: 10.1002/anie.202010159. , in press
(26) Liang, H.-W.; Zhuang, X.; Brüller, S.; Feng, X.; Müllen, K. Hierarchically Porous Carbons with Optimized Nitrogen Doping as Highly Active Electrocatalysts for Oxygen Reduction. *Nat. Commun.* **2014**, *5*, 4973.
(27) Zhao, S.; Kang, D.; Liu, Y.; Wen, Y.; Xie, X.; Yi, H.; Tang, X. Spontaneous Formation of Asymmetric Oxygen Vacancies in Transition-Metal-Doped CeO_2 Nanorods with Improved Activity for Carbonyl Sulfide Hydrolysis. *ACS Catal.* **2020**, *10*, 11739−11750.
(28) Zhao, S.; Wen, Y.; Peng, X.; Mi, Y.; Liu, X.; Liu, Y.; Zhuo, L.; Hu, G.; Luo, J.; Tang, X. Isolated Single-atom Pt Sites for Highly Selective Electrocatalytic Hydrogenation of Formaldehyde to Methanol. *J. Mater. Chem. A* **2020**, *8*, 8913−8919.
(29) Zhao, S.; Wen, Y.; Liu, X.; Pen, X.; Lü, F.; Gao, F.; Xie, X.; Du, C.; Yi, H.; Kang, D.; Tang, X. Formation of Active Oxygen Species on Single-atom Pt Catalyst and Promoted Catalytic Oxidation of Toluene. *Nano Res.* **2020**, *13*, 1544−1551.
(30) Xiaowei, L.; Jean-Charles, R.; Suyuan, Y. Effect of Temperature on Graphite Oxidation Behavior. *Nucl. Eng. Des.* **2004**, *227*, 273−280.
(31) Zhang, B.; Zhang, J.; Shi, J.; Tan, D.; Liu, L.; Zhang, F.; Lu, C.; Su, Z.; Tan, X.; Cheng, X.; Han, B.; Zheng, L.; Zhang, J. Manganese Acting as a High-Performance Heterogeneous Electrocatalyst in Carbon Dioxide Reduction. *Nat. Commun.* **2019**, *10*, 2980.

(32) Gu, X.; Yue, J.; Chen, L.; Liu, S.; Xu, H.; Yang, J.; Qian, Y.; Zhao, X. Coaxial MnO/N-Doped Carbon Nanorods for Advanced Lithium-Ion Battery Anodes. *J. Mater. Chem. A* **2015**, *3*, 1037−1041.
(33) Chen, W.; Pei, J.; He, C.-T.; Wan, J.; Ren, H.; Zhu, Y.; Wang, Y.; Dong, J.; Tian, S.; Cheong, W.-C.; Lu, S.; Zheng, L.; Zheng, X.; Yan, W.; Zhuang, Z.; Chen, C.; Peng, Q.; Wang, D.; Li, Y. Rational Design of Single Molybdenum Atoms Anchored on N-Doped Carbon for Effective Hydrogen Evolution Reaction. *Angew. Chem., Int. Ed.* **2017**, *56*, 16086−16090.
(34) Bak, S.-M.; Shadike, Z.; Lin, R.; Yu, X.; Yang, X.-Q. In Situ/Operando Synchrotron-Based X-ray Techniques for Lithium-Ion Battery Research. *NPG Asia Mater.* **2018**, *10*, 563−580.
(35) Asakura, D.; Hosono, E.; Nanba, Y.; Zhou, H.; Okabayashi, J.; Ban, C.; Glans, P.-A.; Guo, J.; Mizokawa, T.; Chen, G.; Achkar, A. J.; Hawthron, D. G.; Regier, T. Z.; Wadati, H. Material/Element-Dependent Fluorescence-Yield Modes on Soft X-ray Absorption Spectroscopy of Cathode Materials for Li-Ion Batteries. *AIP Adv.* **2016**, *6*, 035105.
(36) Andersen, S. Z.; Čolić, V.; Yang, S.; Schwalbe, J. A.; Nielander, A. C.; McEnaney, J. M.; Enemark-Rasmussen, K.; Baker, J. G.; Singh, A. R.; Rohr, B. A.; Statt, M. J.; Blair, S. J.; Mezzavilla, S.; Kibsgaard, J.; Vesborg, P. C. K.; Cargnello, M.; Bent, S. F.; Jaramillo, T. F.; Stephens, I. E. L.; Nørskov, J. K.; Chorkendorff, I. A Rigorous Electrochemical Ammonia Synthesis Protocol with Quantitative Isotope Measurements. *Nature* **2019**, *570*, 504−508.
(37) Zhu, D.; Zhang, L.; Ruther, R. E.; Hamers, R. J. Photo-Illuminated Diamond as a Solid-State Source of Solvated Electrons in Water for Nitrogen Reduction. *Nat. Mater.* **2013**, *12*, 836−841.
(38) Henkelman, G.; Arnaldsson, A.; Jónsson, H. A Fast and Robust Algorithm for Bader Decomposition of Charge Density. *Comput. Mater. Sci.* **2006**, *36*, 354−360.
(39) Sanville, E.; Kenny, S. D.; Smith, R.; Henkelman, G. Improved Grid-Based Algorithm for Bader Charge Allocation. *J. Comput. Chem.* **2007**, *28*, 899−908.
(40) Lin, S. D.; Gluhoi, A. C.; Nieuwenhuys, B. E. Ammonia Oxidation over $Au/MO_x/\gamma\text{-}Al_2O_3$—Activity, Selectivity and FTIR Measurements. *Catal. Today* **2004**, *90*, 3−14.
(41) Yao, Y.; Zhu, S.; Wang, H.; Li, H.; Shao, M. A Spectroscopic Study on the Nitrogen Electrochemical Reduction Reaction on Gold and Platinum Surfaces. *J. Am. Chem. Soc.* **2018**, *140*, 1496−1501.
(42) Gulaczyk, I.; Kręglewski, M.; Valentin, A. The N−N Stretching Band of Hydrazine. *J. Mol. Spectrosc.* **2003**, *220*, 132−136.